Adsorption (2024) 30:2083–2098
https://doi.org/10.1007/s10450-024-00542-y

Hydrochar-derived activated carbons from poplar and spruce sawdust: synthesis, characteristics and carbon adsorption performance

Sibel Başakçılardan Kabakcı[1] · Başak Karakurt Çevik[1] · Merve Nazlı Borand[1] · Kübra Al[1]

Received: 17 July 2024 / Revised: 3 September 2024 / Accepted: 5 September 2024 / Published online: 26 September 2024

Abstract

The escalating demand for energy across various sectors has led to a significant increase in greenhouse gas emissions, primarily due to the extensive use of fossil fuels. This study addresses the critical need for effective carbon capture adsorbents to mitigate environmental impacts. Bio-based activated carbons, known for their high surface area and pore volume, were synthesized from poplar and spruce sawdust through hydrothermal carbonization (HTC) followed by simultaneous carbonization and activation. HTC, aimed at enriching precursors with oxygen-rich surface functional groups, was conducted at temperatures of 180, 200, and 220 °C for 90 min. This process produced hydrochars that were subsequently activated at 800 °C in the presence of KOH under a nitrogen atmosphere. Remarkably, the activated carbons derived from poplar sawdust hydrochar (at a HTC temperature of 200 °C) and spruce sawdust hydrochar (at a HTC temperature of 220 °C) demonstrate superior specific surface areas of 1680.59 and 1231.57 m^2/g, along with total pore volumes of 0.87 and 0.62 cm^3/g, respectively. Moreover, both poplar and spruce hydrochar-based activated carbons exhibit high CO_2 adsorption capacities of 3.75 and 3.43 mmol/g, respectively, at 24.85 °C and 1 atm. Their CH_4 adsorption capacities are 1.52 and 1.42 mmol/g, respectively, under the same conditions. This work highlights the potential of bio-based activated hydrochars in applications such as indoor air quality improvement and industrial flue gas treatment, emphasizing the importance of pretreatment and activation conditions in optimizing adsorbent performance.

Keywords Hydrothermal carbonization · Activated carbon · Hydrochar · CO_2 adsorption · CH_4 adsorption

1 Introduction

The dramatic increase in energy demand across transportation, electricity production, industry, and the commercial and residential sectors has led to a significant rise in greenhouse gas emissions, primarily due to the reliance on fossil fuels [1–3]. This increase in emissions poses serious challenges, including extreme weather events (such as elevated average temperatures, droughts, heatwaves, and floods), sea level rise, coral reef bleaching, species extinctions (including insects, plants, and animals), and reduced crop production. Among greenhouse gases, carbon dioxide (CO_2) and methane (CH_4) are emitted in large quantities as a result of human activities. Developing and adopting low-emission technologies, as well as carbon capture and storage solutions, are crucial to achieving the target of limiting global warming to 1.5 °C above pre-industrial levels [4].

Gas adsorption technologies have garnered significant attention due to several advantageous features, including a variety of adsorbent options, the ability to operate under atmospheric conditions, low energy requirements, and cost-effectiveness. [5, 6]. The performance of gas adsorption is highly dependent on the type and properties of the adsorbents [7]. Porous materials, such as metal–organic frameworks, clays, zeolites, and carbon-based materials, are particularly effective due to their large surface area, total pore volume, and high adsorption capacity [8]. Activated carbons, in particular, are exceptional adsorbents due to their porous structure, controllable pore size distribution, thermal

✉ Merve Nazlı Borand
nazli.erdonmez@yalova.edu.tr

Sibel Başakçılardan Kabakcı
sibel.kabakci@yalova.edu.tr

Başak Karakurt Çevik
basak.cevik@yalova.edu.tr

Kübra Al
kubra.al@yalova.edu.tr

[1] Faculty of Engineering, Energy Systems Engineering Department, Yalova University, 77200 Yalova, Turkey

stability, and the presence of oxygen-rich functional groups. Activated carbon is a carbon-rich adsorbent synthesized from carbonaceous material such as petroleum coke, coal, and biomass using physical methods, chemical methods, or a combination of both [9]. In a typical synthesis process, the carbon-rich material is first thermally treated—through methods such as torrefaction, pyrolysis, gasification, or hydrothermal carbonization—to increase its carbon content [10]. Next, the porosity is developed and the structure of the char is modified through activation. Carbonization and activation can also be performed simultaneously. Physical activation involves treating the char with an activating agent such as CO_2, steam, air, or O_2 at elevated temperatures. In contrast, chemical activation involves treating the precursor with a chemical activating agent, such as KOH, NaOH, $CaCl_2$, H_3PO_4, K_2FeO_4, Na_2CO_3, $ZnCl_2$, or $FeCl_3$ [11, 12], and heating it to a temperature of 500–900 °C under an inert atmosphere. After chemical activation, further treatment, including washing and drying, is required to remove the excess activator. Among chemical activators, KOH is the most commonly used due to its ability to produce activated carbons with high surface area, large pore volumes, and a tunable microporous structure [13]. Chemically activated carbonaceous materials typically exhibit higher surface areas and more surface functional groups compared to physically activated carbons [14]. The surface characteristics, porous structure, and physicochemical properties of chemically activated carbons are influenced by factors such as the type of precursor, carbonization conditions, and the type and conditions of activation [13].

Bio-based activated carbons have gained significant attention for their use in energy and environmental applications [15]. The growing interest in these materials is attributed to their resilience, high surface area, and pore volume, ease of production and scaling, and the simplicity with which their physicochemical characteristics can be modulated [15–17]. The porosity and structural properties of bio-based porous carbonaceous materials are crucial for gas storage and separation applications [18, 19]. Their large surface area, high pore volume, and availability of functional groups make bio-based activated carbons important adsorbents. In contrast, activated carbon derived from coal has an adsorption rate that is 2 to 50 times slower than that of activated carbon derived from woody biomass. This difference is primarily due to the naturally porous and fibrous structure of biomass, which provides a significantly higher external surface area [12, 20].

Pretreating the biomass prior to carbonization/activation significantly influences the characteristics of activated carbon and its adsorption yield [21, 22]. Hydrothermal carbonization (HTC) is a well-known pretreatment method, which has several advantages over other carbon enrichment processes, especially in terms of energy consumption [23]. HTC is performed at temperatures around 150–350 °C, under self-increasing pressure or high pressure (2–10 MPa) for a certain time [24–26]. During HTC, several reactions including hydrolysis, dehydration, decarboxylation, condensation, and polymerization, occur simultaneously in a complex network. Hydrochar, the solid product of treatment, is much more stable than biomass, and it has more oxygenated functional groups [27]. HTC is preferable to pyrolysis for char synthesis because it can utilize moisture-rich biomass without requiring drying, whereas pyrolysis requires dry biomass. [28]. The physicochemical properties, surface characteristics, and thermal stability of hydrochar are influenced by HTC parameters such as temperature, retention time, type of biomass, and biomass-to-water ratio [23, 29, 30].

This study highlights the potential of converting wood sawdust into high-value activated carbons for environmental applications, emphasizing the critical roles of HTC and activation processes in shaping the properties and performance of the adsorbents. The experimental objectives are threefold: (1) to produce bio-based microporous activated carbons using hydrothermal carbonization and carbonization-activation methods, (2) to examine the effects of hydrochars obtained at varying HTC temperatures on the properties of the activated carbons, and (3) to assess the CO_2 and CH_4 adsorption capacities of the activated carbons with the highest surface area and micropore volume. While the production of activated carbon is well-established, the novelty of this study lies in the integration of specific process conditions, including the selection of hardwood (poplar sawdust) and softwood (spruce sawdust) as biomass feedstocks, the implementation of a hydrothermal carbonization pretreatment, and the fine-tuning of activation parameters. These tailored conditions have been optimized to yield activated carbons with unique microporous structures and enhanced surface functionalities, specifically designed for effective CO_2 and CH_4 adsorption.

Poplar and spruce sawdust were selected as biomass raw materials due to their abundance as byproducts of woodworking operations (such as sawing, sanding, and milling) and their significant production volumes, particularly in regions with extensive wood processing industries. Utilizing sawdust as a feedstock presents an opportunity to convert this lignocellulosic waste—typically burned for energy—into activated carbon, thereby enhancing its value and contributing to the bio-based economy.

2 Materials and methods

2.1 Materials

Poplar and spruce wood sawdust samples were supplied by local wood processing industries located in the South

Marmara region. All waste wood samples were dried (105 °C for 24 h) to prevent samples from rotting. After grinding, samples were sieved using Retsch As 200 vibrating sieve (Verder Group, Germany) to have a uniform particle size of 250 µm. All chemicals used in both the analysis and treatments were of analytical grade and used without further purification.

2.2 Hydrothermal carbonization

Hydrothermal carbonization of poplar and spruce wood sawdust samples was performed in a 250 ml non-stirred, temperature-controlled, stainless-steel batch reactor. HTC conditions were kept the same and constant (residence time: 90 min, biomass/water: 10 g/40 ml) to accurately compare the structural properties of hydrochars. The experiments were carried out at 180, 200, and 220 °C. Each experiment was done in triplicate. The residence time (90 min) included the preheating of the reactor to the desired temperature but excluded the cooling period. At the end of the pretreatment, the reactor was cooled rapidly using an ice bath. Gases formed during the pretreatment were not collected. The mixture was then filtered to separate hydrochar. The hydrochars were washed with deionized water and then dried in an oven at 105 °C for 24 h. Each hydrochar sample was named based on its HTC temperature. Hydrochars obtained from poplar wood sawdust at 180, 200, and 220 °C were named HTP180, HTP200, and HTP220, respectively, while those obtained from spruce wood sawdust were named HTS180, HTS200, and HTS220.

2.3 Preparation of activated carbon

Each hydrochar sample was mixed with KOH (Merck, Germany) at a ratio of 1:2 (w:w), separately. Then, the mixture was placed in a horizontal tubular furnace, and heated at a rate of 10 °C/min to 800 °C and maintained at this temperature for 1 h. During heating and cooling, the tubular furnace was continually flushed with nitrogen gas. After activation, the activated carbon sample was washed with 0.1 M HCl (Isolab, Germany) and deionized water. The sample was dried at 105 °C for 24 h. The activated carbons obtained from poplar wood sawdust and spruce wood sawdust were named ACP and ACS, respectively. Activated carbons prepared from the hydrochars of poplar wood sawdust were named ACHTP180, ACHTP200, and ACHTP220, while those obtained from the hydrochars of spruce wood sawdust were named ACHTS180, ACHTS200, and ACHTS220.

2.4 Characterization

Determination of C, H, N, and S content of dry samples was done using an elemental analyzer (LECO CHNS-932, LECO, USA). The moisture content of the sample was assessed by oven-drying it at 105 °C until a constant weight was observed, while the ash content was measured by oxidizing the dry sample at 575 °C, following the NREL/TP-510–42622 laboratory analytical procedure [31]. The proximate analysis and thermal behavior of the samples were evaluated using a thermogravimetric analyzer (Seiko TG/DTA 6300, Seiko Instruments Inc., JAPAN). The proximate analysis was conducted using the thermogravimetric method developed by Garcia et al. [32]. To ensure accuracy, the ash content obtained from this method was compared with that determined using the NREL method. For the thermal behavior analysis, samples were heated from room temperature to 900 °C at a heating rate of 40 °C /min and maintained for 7 min. Analyses were carried out under air and nitrogen atmospheres.

Fourier Transform Infrared (FTIR) spectra of hydrochars and activated carbons were obtained using an FTIR analyser (Perkin Elmer, United States) coupled with a universal attenuated total reflectance (ATR) sampling device with a diamond crystal. The spectra were recorded with a resolution of 4 cm^{-1}, in the range from 400 to 4000 cm^{-1}.

The surface morphologies of hydrochars and activated carbons were investigated by Inspect S50 FEI Inc., USA Scanning electron microscope (SEM). Samples were scanned under 20 kV in the high vacuum mode using secondary electrons with different magnifications.

The X-ray diffraction (XRD) patterns of hydrochars and activated carbons were collected using X-Ray diffractometer (Rigaku Smartlab, Japan), operating at 40kVand 30 mA, with a scan range of 10 to 80°, a step width of 0.02° and a scan speed of 3.035°/min. The crystallinity index (CrI) was calculated using,

$$CrI\,(\%) = (I_{002} - I_{am})/I_{002} \times 100 \quad (1)$$

where, I_{002} is the maximum intensity of the 002 plane (at 2q = 22.5°) and I_{am} is the height of the minimum between 002 and 101 peaks [33, 34].

The surface area and pore structure characteristics of activated carbons were determined using Quantachrome-Autosorb iQ BET analyzer (Anton Paar, Austria) at 77 K in the relative pressure range of 0.001 and 0.99. Before the analysis, the samples were degassed at 180 °C for 24 h. The nonlocal density functional theory model was used to determine the pore size distribution based on N_2 adsorption in the slit pore equilibrium model at 77 K.

Micromeritics TriStar II 3020 analyzer (Micromeritics Inc., USA) was used to observe CO_2 and CH_4 adsorption–desorption at 24.85 °C up to 1 bar. Prior to analysis, the samples were degassed at 179.85 °C for 24 h.

Table 1 FTIR band assignments of biomass samples and their hydrochars [36–38]

Peak	Spruce	HTS180	HTS200	HTS220	Band assignment
	Wavelength (cm^{-1})				
1	3341	3341	3340	3339	O–H stretching vibration in aliphatic and phenolic structures (C, H, L)*
2	2924	2900	2898	2900	C–H stretching vibration in methyl and methylene groups (C, H, L)
3	1730	1728	1728	1728	C=O stretching vibration in ketones and carboxyl groups (H,L)
4	1635	1635	1635	1605	Aromatic skeletal vibration and C=O stretching vibration (H, L)
5	1510	1509	1509	1508	Aromatic ring stretching vibration (L)
6	1425	1423	1423	1423	Symmetric CH_2 bending vibration, symmetric stretching vibration of carboxyl group (C, H, L)
7	1370	1370	1370	1369	Aliphatic C–H deformation in methyl groups (C, H, L)
8	1263	1264	1264	1264	Guaiacyl ring breathing with C=O stretching vibration (L)
9	1023	1028	1028	1028	C–O deformation in alcohols and aromatic C–H in-plane deformation in guaiacyl units (C, H, L)
Peak	Poplar	HTP180	HTP200	HTP220	
	Wavelength (cm^{-1})				
1	3334	3339	3335	3333	O–H stretching vibration in aliphatic and phenolic structures (C, H, L)
2	2899	2901	2917	2900	C–H stretching vibration in methyl and methylene groups (C, H, L)
3	1734	1732	1736	1736	C = O stretching vibration in ketones and carboxyl groups (H,L)
4	1594	1595	1595	1595	Aromatic skeleton vibrations (L)
5	1506	1505	1506	1506	Aromatic ring stretching vibration (L)
6	1422	1423	1422	1422	Symmetric CH_2 bending vibration, symmetric stretching vibration of carboxyl group (C, H, L)
7	1320	1317	1317	1317	Syringyl ring breating with C–O stretching vibration (L)
8	1231	1239	1235	1237	C–O stretching of guaiacyl unit
9	1030	1029	1030	1030	C–O deformation in alcohols and aromatic C–H in-plane deformation in guaiacyl units (C, H, L)

*C: cellulose, H: hemicellulose, L: Lignin

3 Results and discussion

3.1 Properties of hydrochars

The elemental compositions of polar and spruce sawdust, along with their corresponding hydrochars produced at different hydrothermal temperatures, were analyzed to assess the effects of hydrothermal treatment on biomass transformation (Table A1). Poplar sawdust exhibited initial carbon and hydrogen contents of 43,70% and 5,97%, respectively, with oxygen being the predominant component (47,63%). In comparison, spruce sawdust had slightly higher carbon content (47,59%) and lower hydrogen (3,50%), with a similar oxygen proportion of 47,51%. Upon hydrothermal treatment, the resulting hydrochars generally showed increased carbon content, suggesting carbon enrichment, while hydrogen content decreased, indicative of partial hydrogen removal. As observed in other studies, HTC of woody biomass generally results in carbon enrichment and hydrogen decrease [35]. The highest carbon enrichment for poplar sawdust hydrochars occurred at 200 °C, with a carbon content of 48,39%. In contrast, for spruce sawdust hydrochars, the highest carbon enrichment was observed at 220 °C, reaching a carbon content of 49,22%. The ash content in all hydrochars remained relatively low (< 2% for poplar hydrochars, < 1,4 for spruce hydrochars). This reduction in ash content is primarily due to the dissolution of ash-forming minerals under HTC conditions, which reduces their presence in the solid hydrochar and contributes to the overall efficiency of the process. These changes are consistent with the alteration in the elemental composition of the biomass under hydrothermal conditions, as evidenced by the accompanying Van Krevelen diagram (see Fig. 1.) illustrating shifts in H/C and O/C ratios.

The extent of the H/C and O/C ratios in a Van Krevelen diagram indicates the degree of dehydration, deoxygenation, and demethanation that occur during HTC, depending on the process conditions [39]. In the diagram (see in Fig. 1.), dehydration which eliminate the hydroxyl groups, follows a pathway that reduces both H/C and O/C atomic ratios from the top right to the bottom left. Dehydration is the main reaction for HTP180, HTP200 and HTP220. Decarboxylation, which carboxyl and carbonyl groups leave the structure, follows a pathway from the bottom right to upper left corner. During decarboxylation, H/C ratio increases and the O/C ratio decreases, which was observed in HTS220. Li

et al. [40] found that both decarboxylation and dehydration reactions occurred during the HTC of pinewood sawdust at 220 °C.

The mass yields of hydrochars did not vary significantly within different HTC temperatures however the mass yield of spruce hydrochars (90,3%) were higher than that of poplar hydrochars (87,7%). This is mainly due to structural difference between hardwoods and softwoods [41]. In a lignocellulosic biomass, the amount of component degradation follows the order hemicellulose > cellulose > lignin at the same hydrothermal conditions [42]. Hemicellulose, being an amorphous polymer, is easily degraded under hydrothermal conditions. For both hardwoods and softwoods, hemicellulose is hydrolyzed at temperatures around 180 °C [43], and cellulose at higher temperatures. Lignin, on the other hand, is a more stable phenylpropanoid structure that is hardly decompose under hydrothermal conditions. In hardwoods, hemicellulose content is higher, and the lignin content is usually lower compared to softwoods. Therefore, HTC has slightly higher effect on hardwood compared to softwood [44]. Moreover, monolignols in hardwood lignins are coniferyl and sinapyl alcohols (which appear as guaiacyl and syringyl monomer structures respectively) in variable contents, while softwood lignins are mainly composed of coniferyl alcohol (guaiacyl monomer). Due to more condensed structure, softwoods are more resistant to lignin degradation [45].

FTIR analysis was performed to evaluate the effect of different HTC temperatures on the functional groups of hydrochars (see Supplementary Fig. A1). According to the FTIR spectra, the biomass samples and their corresponding hydrochars showed the same functional groups, although the intensity of certain peaks of the poplar sawdust and spruce sawdust were modified by HTC. The intensity of -OH stretching vibration of phenols, alcohols, and carboxylic acids (centered at 3400 cm^{-1}) was more in spruce hydrochars, which was also supported by high oxygen content. All poplar-derived and spruce-derived hydrochars showed aliphatic C–H stretching vibration around 2800–3000 cm^{-1} with higher intensity compared to their biomass source. In spruce-derived hydrochars, C=O stretching vibration of guaiacyl unit at 1263 cm^{-1}, C = C stretching of aromatic rings at 1510 cm^{-1}, C–H bending vibration of cellulose at 1423 cm^{-1}, C–O deformation in primary alcohols and aromatic C–H in-plane deformation at 1030 cm^{-1} were observed with higher intensities compared to that of spruce hydrochar. For both spruce-derived hydrochars and poplar-derived hydrochars, HTC obviously enhanced the aromaticity, which was also shown by [44]. As the peak intensities of poplar-derived hydrochars were compared, HTP200 appeared to have the highest intensity in all bands.

The thermal stability of both poplar sawdust and spruce sawdust, along with their corresponding hydrochars, was investigated using thermogravimetric analysis under an N_2 atmosphere. (see Supplementary Fig. A2). Whether hardwood or softwood, thermal degradation behavior under an inert atmosphere is similar to those reported in the literature [46, 47]. A typical pattern is observed in all derivative thermogravimetry (DTG) curves within 80–130 °C due to dehydration and removal of light gases [48]. A subsequent thermal degradation occurs at 200–420 °C, where the decomposition of hemicellulose and cellulose takes place.

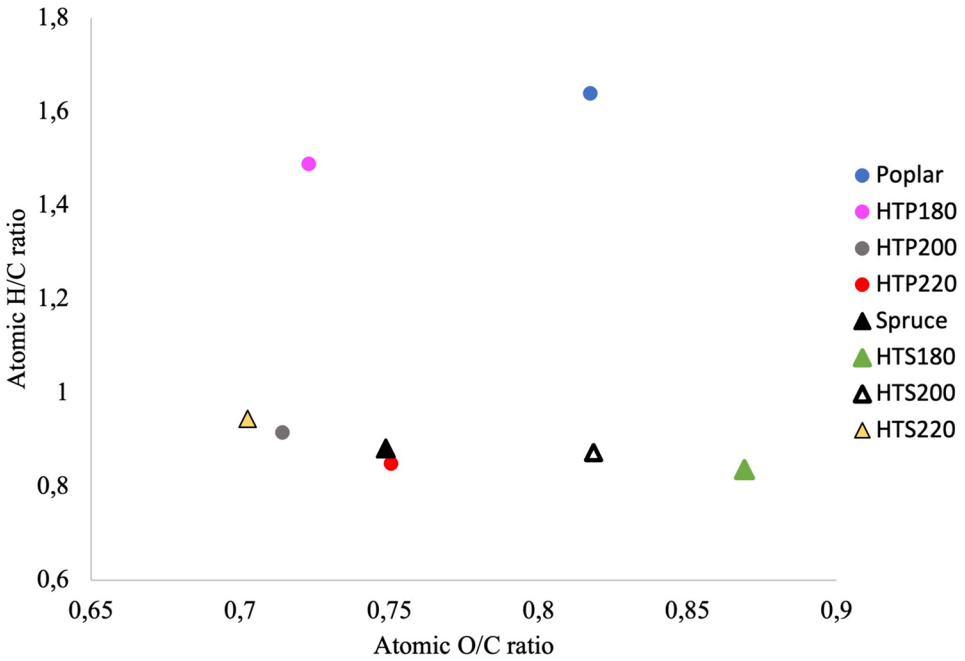

Fig. 1 Van Krevelen diagram for poplar sawdust, spruce sawdust, and their hydrochars

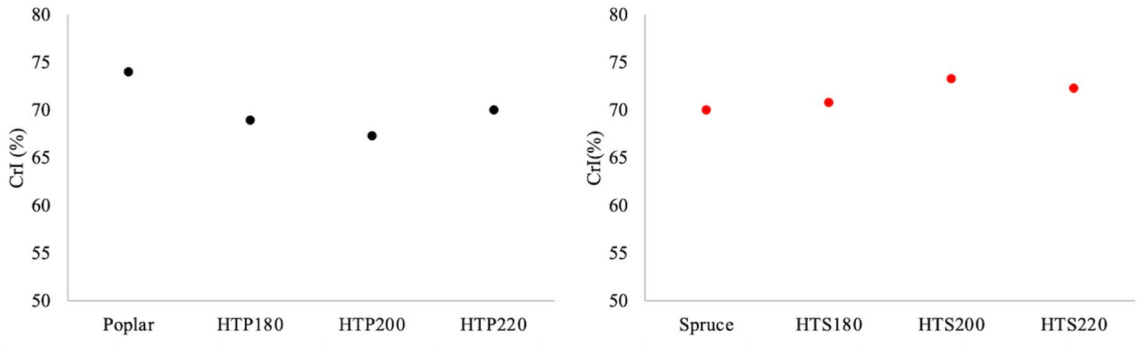

Fig. 2 Crystallinity index of poplar, spruce, and their resultant hydrochars

The shoulder before the peak is associated with hemicellulose degradation, while the main peak is due to the thermal decomposition of cellulose. Whereas lignin is decomposed in a wider temperature range (200–900 °C), without showing a characteristic DTG peak [49]. The temperature of maximum mass loss rate (T_{max}) is 397 °C and 384 °C for spruce sawdust and poplar sawdust, respectively. As in this study, Ding et al. [50] and He et al. [44] also observed that the T_{max} of softwood samples was higher than that of hardwood samples.

Regardless of the biomass source, HTC has enhanced the thermal stability of hydrochars. While the increase in T_{max} values for poplar-derived hydrochars ranged between 18.7 and 19.9 °C, the temperature shift for spruce-derived hydrochars ranged between 8.4 and 9.3 °C. The extent to which hemicellulose decomposes at low HTC temperatures affects the T_{max} value. This can be explained by the difference in both the amount and structure of hemicellulose in hardwood and softwood. Hemicellulose content is higher in hardwood compared to softwood. At the same time, the basic components of hemicellulose in hardwood and softwood are also different from each other. While hardwood celluloses contain more glucomannan and glucuronoxylan, softwood hemicelluloses contain arabino glucuronoxylan, galactoglucomannan, and glucomannan. This makes hardwood more vulnerable to thermal treatments. This observation is also supported by X-ray diffraction results.

The x-ray diffraction patterns of all samples exhibit diffraction peaks at 15° (101), 22.5° (002), and 34.5° (040) (see Supplementary Fig. A3). In a lignocellulosic biomass, cellulose is in the form of both crystalline and amorphous, while lignin and hemicellulose have amorphous structure [51]. Based on HTC severity, hemicellulose, amorphous cellulose, and lignin partially decompose during HTC, and thus change the crystallinity index [52]. As seen in Fig. 2, the crystallinity index of poplar sawdust is higher than that of spruce, which is also observed by Popescu et al. [53] and Bay et al. [54]. Although softwoods have a higher cellulose content than hardwoods, the arrangement and orientation of cellulose microfibrils within the cell walls of hardwoods are more complex [55], which may lead to a higher degree of crystallinity. For spruce-derived hydrochars, the crystallinity index tends to increase slightly due to loss in amorphous structure. For poplar-derived hydrochars, the crystallinity index slightly decreases at low and moderate HTC temperatures. A decrease in the intensity of the diffraction peak at 22.5° (I_{002}) for HTP200 denotes the partial decomposition of cellulose. In contrast, no change in the peak intensity of I_{002} is observed in the x-ray diffraction of spruce-derived hydrochars. A similar observation was made by He et al. [44], showing that the peak intensity of cellulose in pinewood remained almost stable at 220 °C, while in poplar wood, the peak intensity decreased at 200 °C.

The surface morphology of raw samples and hydrochars, which was observed by SEM, can be seen in Supplementary Fig. A4. No pores or cavities were detected on the surface of raw poplar and spruce sawdust. Due to HTC reactions, the surface changes occurred as observed in the SEM images of hydrochars. Upon increasing HTC temperature, small pores, and cracks can be seen on the surface of HTP180, HTP200, and HTP220. Unlike poplar, spruce sawdust showed longitudinal tubes with fewer pores. As explained by Nitsos et al. [56], resistant nature of softwood lignin results in rough surface without any pseudolignin formation or pores even at high HTC severity.

3.2 Activated carbons prepared from hydrochar

As a carbon-enriched precursor, hydrochars were chemically activated with KOH using a one-step method, where the precursor and activator were directly pyrolyzed at 800 °C. As explained extensively in the study of Chen et al. [57], in one-step KOH activation, KOH not only reacts with carbon, it also reacts with oxygen-containing species, depending on KOH:precursor ratio and temperature. Under conditions where KOH is in excess relative to the precursor and the temperature is high (700–800 °C), reactions between KOH and carbon fragments are enhanced compared to those

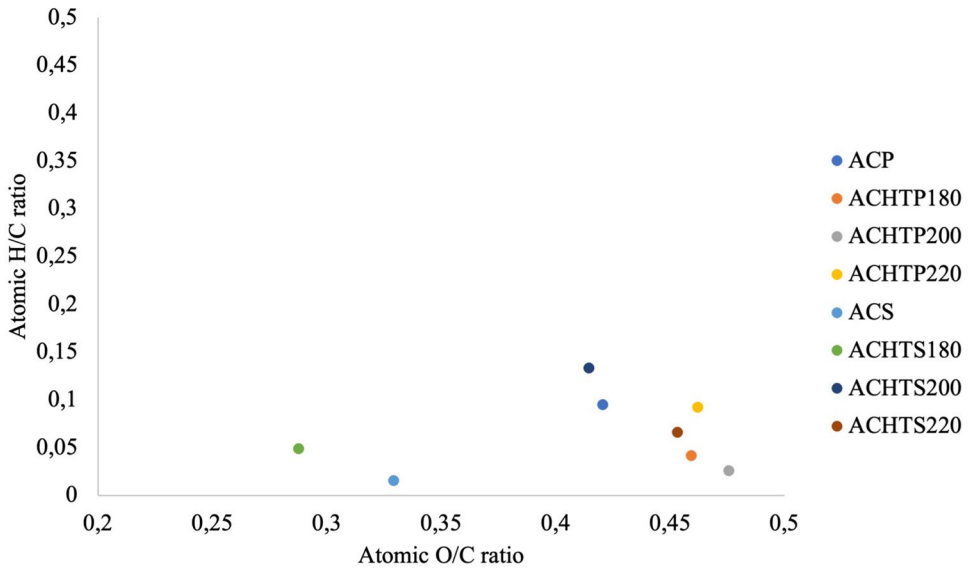

Fig. 3 Van Krevelen diagram for activated carbons

between KOH and the oxygen-containing functional groups of the precursor. While those reactions generate spaces in the structure, more OH^- groups attach to those sites, providing a developed porosity and more oxygen-containing functional groups. One-step activation and pyrolysis process result in a decrease in mass, which in turn changes the content of C, H, and O. In our study, atomic H/C and O/C ratios were changed significantly due to deoxygenation and dehydrogenation reactions that predominate at temperatures as high as 800 °C (see in Van Krevelen diagram shown in Fig. 3). The carbon content of all wood-derived samples increased, and the hydrogen content decreased. Based on elemental analysis, the carbon content of activated carbons derived from poplar is slightly lower than those derived from spruce. Activated carbons derived from poplar and its hydrochars contain N in small fractions (less than %0,4). All activated carbons contain S less than 0,7% by weight. Elemental analysis of the activated carbons revealed relatively high oxygen content, as indicated by a high O/C ratio in the Van Krevelen diagram, suggesting the presence of oxygen-containing functional groups. As also observed in FTIR spectra of the activated carbons (Fig. 4.), most of the oxygen is in the structure of surface functional groups. Oxygen-containing functional groups are known to increase the adsorption ability of activated carbons [58–60].

Figure 4 shows the FTIR spectra of the wood-derived activated carbons. The very low hydrogen content in all samples after activation is noticed by the absence of the O–H stretching at 3200–3600 cm^{-1}, and the lower intensity of the C–H stretching at 2650 cm^{-1}, 1990 cm^{-1} and 1860 cm^{-1}. In all spectra, C–O stretching in ketene groups appears at 2328–2334 cm^{-1} [61]. The intense peak at 2112–2116 cm^{-1} is assigned to C=C=C stretching [62]. C=O stretching vibration of ketones, aldehydes, and carboxyl groups at 1710 cm^{-1} was only detected in the spectra of ACP. C=C stretching (due to aromatization) and C–O stretching (in carboxyl and aldehyde structures) appear at 1550–1559 cm^{-1} in all spectra [63, 64]. C–O bending (in alcohol, ether, and carboxylic groups) appears at 1000–1200 cm^{-1} with different intensities [65].

X-ray diffraction patterns of all activated carbons are shown in Fig. 5. The broad diffraction peak at around 24° shows the 002 plane of graphitic carbon. The diffraction patterns show another wide but low-intense diffraction peak located at around 44°, which denotes 100 plane of disordered graphite structure. Based on diffraction patterns, amorphous structure is dominant in all structures. The temperature at which hydrochar was obtained did not affect the structure of activated carbon.

SEM images of all activated carbons are shown in Fig. 6, with additional images of poplar and spruce sawdust samples and their corresponding hydrochars provided in Supplementary Fig. A4. Initially, both poplar and spruce sawdust exhibited smooth surfaces; however, tiny pores were visible in the poplar, while the spruce showed no visible pores. During HTC at 180 °C, the structure of poplar changed significantly due to the partial removal of hemicellulose, making the pores more pronounced, whereas the morphology of spruce remained largely unchanged. As the HTC temperature increased to 200 °C, both samples developed rougher surfaces with numerous pores. Poplar hydrochars exhibited a higher density of pores compared to spruce hydrochars. At 220 °C, poplar hydrochars began to exhibit microsphere formations within some of the pores, likely due to lignin repolymerization. In contrast, spruce hydrochars at 220 °C developed small pores, indicating a morphological change at this higher temperature.

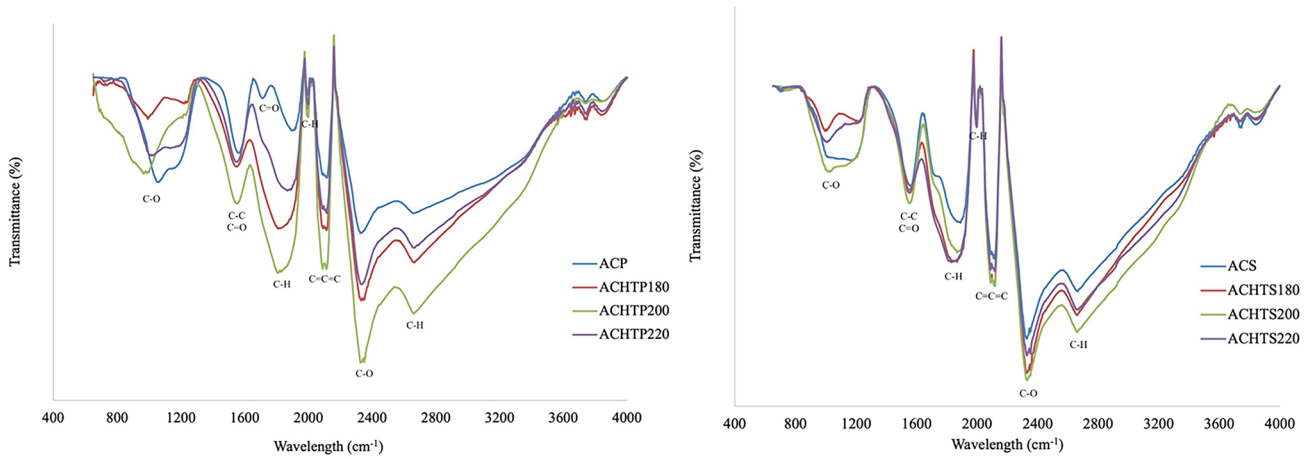

Fig. 4 FTIR spectra of activated carbons

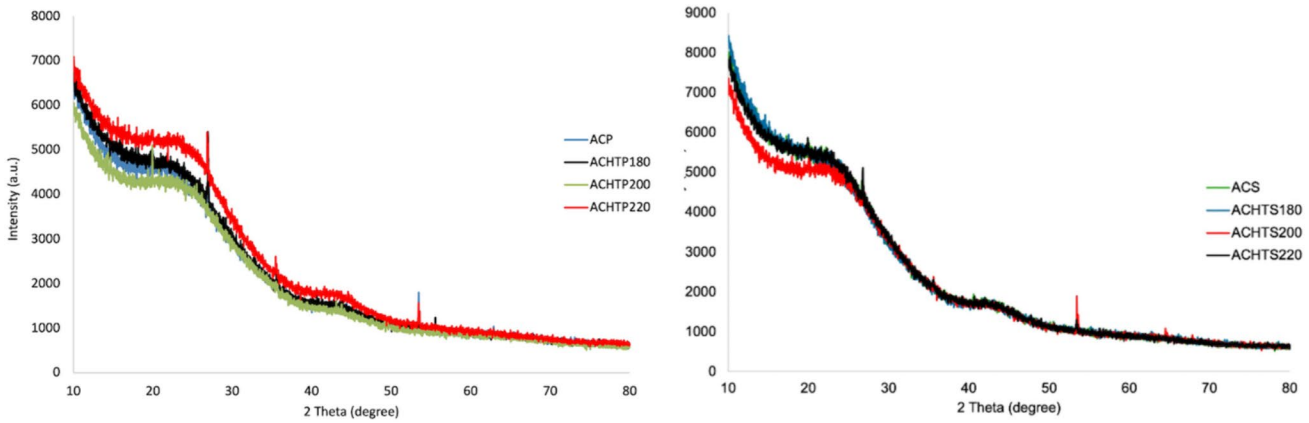

Fig. 5 X-ray diffraction of activated carbons

Following the removal of most carbonaceous structures at 800 °C and subsequent activation with KOH, porous activated carbons with varying shapes, pore sizes, and wall thicknesses were obtained. Since the one-step pyrolysis-activation process conditions were consistent, the differences in porosity among the activated carbons can be attributed to the nature of the hydrochars. Compared to spruce-derived activated hydrochars, poplar-derived activated hydrochars exhibited a more sponge-like structure, characterized by well-distributed and well-developed pores (see Fig. 6). However, in the activated hydrochar of poplar at 220 °C, some pores appeared to be clogged, likely due to the deposition or condensation of lignin-derived substances during the carbonization process. This contrasts with more well-developed porous structure observed in spruce-derived activated hydrochar at 220 °C, showing the significant impact of precursor composition and HTC conditions on the final pore development.

The pore characteristics of activated carbons are given in Table 2. Since the activation process was carried out under the same conditions for all samples, only the precursor properties affected the surface area and pore structure. The surface areas of activated carbons vary between 787,06 m^2/g and 1680 m^2/g. All activated carbons mainly have a microporous structure and mesopores are less. The BET surface area of ACP is higher compared to ACS. However, ACS has more micropore volume in the total volume. The difference in surface area and pore structure between ACP and ACS can be attributed to the inherent differences between hardwoods and softwoods. Hardwoods like poplar are more vulnerable to thermal treatment, leading to a greater release of volatiles, which creates more pores. Additionally, hardwoods possess vascular tubes that act as natural pores, a feature absent in softwoods like spruce. It was also observed in Shrestha [64] that activated carbons derived from hardwoods have a higher specific surface area and larger pore diameter

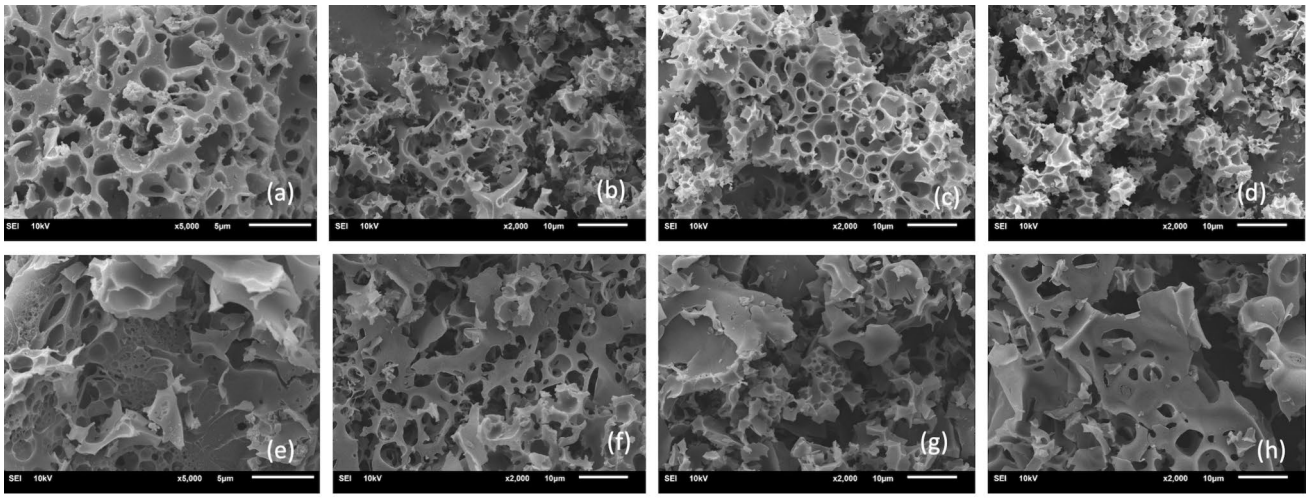

Fig. 6 SEM images of **a** ACP, **b** ACHTP180, **c** ACHTP200, **d** ACHTP220, **e** ACS, **f** ACHTS180, **g** ACHTS200, **h** ACHTS220

Table 2 The porous characteristics of activated carbons

Sample	S_{BET} (m^2/g)	r_{avr} (nm)	V_{total} (cm^3/g)	V_{micro} (cm^3/g)	S_{micro} (m^2/g)	S_{micro}/S_{BET} (-)	V_{micro}/V_{total} (-)
ACP	1248,87	1,09	0,68	0,46	1071,29	0,86	0,67
ACHTP180	1218,73	1,09	0,66	0,45	1044,94	0,86	0,67
ACHTP200	1680,59	1,04	0,87	0,64	1498,58	0,89	0,73
ACHTP220	1049,69	0,98	0,52	0,39	911,32	0,87	0,76
ACS	1192,28	0,98	0,59	0,45	1049,00	0,88	0,76
ACHTS180	1176,80	1,01	0,60	0,43	1012,72	0,86	0,72
ACHTS200	787,06	1,02	0,40	0,30	707,49	0,90	0,75
ACHTS220	1231,57	1,01	0,62	0,44	1033,15	0,84	0,71

than those derived from softwoods. Liang et al. [66] synthesized poplar-based activated carbon at the same conditions with a specific surface area of 1486,2 m^2/g and 0,767 cm^3/g. In contrast, Guy et al. [67] used spruce bark to prepare activated carbon under identical conditions (800 °C and 1 h activation with KOH at a 1:2 ratio) and obtained a specific surface area of 572 m^2/g. Among the activated carbons derived from poplar sawdust hydrochars, ACHTP200 exhibits the highest surface area (1680 m^2/g) with an average pore diameter of 2,08 nm. In comparison, among the activated carbons obtained from spruce sawdust hydrochar, ACHTS220 has the highest surface area (1231,57 m^2/g). The higher surface area observed in ACHTP200 at the mild HTC temperature of 200 °C may be due to the limited thermal degradation at this temperature, which prevents significant lignin condensation within the pores. The differences in lignin structure between hardwoods and softwoods also play a crucial role. Softwoods like spruce contain primarily guaiacyl units, which are more resistant to cleavage and more thermally stable compared to the syringyl units found in hardwoods like poplar. This stability allows for more controlled pore development at higher temperatures, such as 220 °C, without significant degradation. In contrast, the syringyl units in poplar may degrade more readily, leading to more pores at lower temperatures but potentially causing lignin condensation and reduced porosity at higher temperatures.

N_2 adsorption isotherms at 77 K are shown in Fig. 7. All N_2 adsorption isotherms of hardwood-derived activated carbons show a steep increase at very low relative pressures indicating the presence of micropores. A wide hysteresis loop is observed at $0{,}5 < P/P_0 < 1$, which reflects the mesoporous structures. Similarly, ACP and ACHTP180 show a smaller hysteresis loop (as compared to ACHTP200). The hysteresis loop observed in the N_2 adsorption isotherm of ACP, ACHTP180, and ACHTP 200 is a type H4 hysteresis (as classified by IUPAC), showing that adsorption is a composite of Type I and Type II isotherms. Among the hardwood-derived activated carbons, ACHTP200 has the highest N_2 adsorption capacity, which is mainly due to its high surface area and micropore volume (as seen in Table 4). ACHTP220 represented Type I isotherm, which is a characteristic of adsorbents that have micropores with small

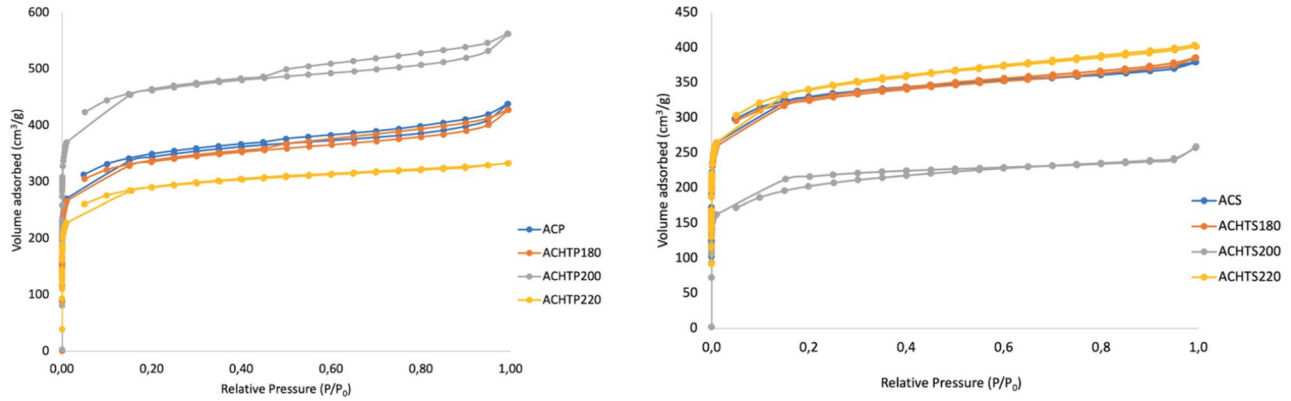

Fig. 7 N_2 adsorption–desorption isotherms at 77 K

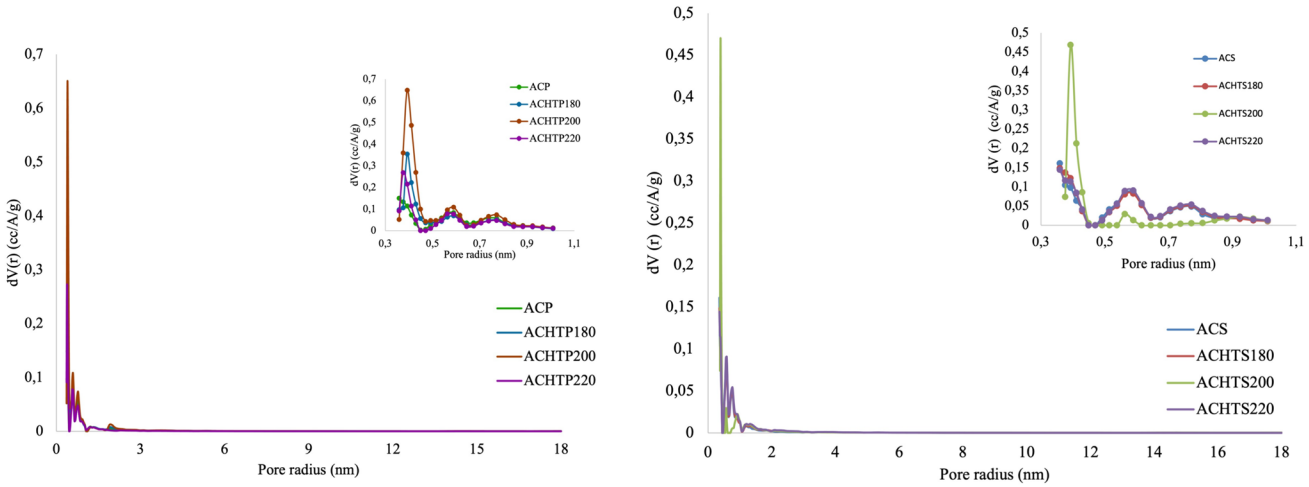

Fig. 8 Pore size distribution calculated by using nonlocal density functional theory (NLDFT) for N_2 adsorption at 77 K

external surfaces. The low adsorption is due to micropore volume rather than internal surface area [68].

All softwood-derived activated carbons showed a combination of Type I and Type II isotherm, while a steep uptake of N_2 is observed at very low relative pressures ($P/P_0 < 0{,}05$), there exists a slight increase in the amount of adsorbed nitrogen at higher relative pressures ($1 > P/P_0 > 0{,}1$). The N_2 adsorption isotherms of ACS, ACHTS180, and ACHTS220 are reversible, without a hysteresis loop.

Figure 8 shows the pore size distribution based on the NLDFT method from N_2 adsorption at 77 K. All the activated carbons contain micropores, which show three peak points around 0,39 nm, 0,58 nm, and 0,77 nm. In the case of poplar-based activated carbons, the majority of the micropores are in the range of 0,35–0,49 nm. Hydrothermal carbonization applied to poplar prior to activation enhanced the micropore formation, which is evident from the maxima of the pore radius distribution curves. For spruce-based activated carbons, except ACHTS200, all activated carbons have micropores in a similar range of pore radius.

3.3 CO_2 and CH_4 adsorption capacity of activated carbons

The activated carbons with the highest surface area, namely ACHTP200, and ACHTS220, were selected for CO_2 and CH_4 adsorption at 25 °C. The adsorption isotherms of CO_2 and CH_4 on ACHTP200 and ACHTS220 at 25 °C are shown in Fig. 9. For both activated carbons, the molar amount of CO_2 and CH_4 per mass of adsorbent increased with pressure (see in Fig. 8). Moreover, both CO_2 and CH_4 adsorption–desorption isotherms were lacking hysteresis, denoting physical adsorption occurring on the surface. Both ACHTP200 and ACHTS220 adsorbed CO_2 more than CH_4, mainly due to the quadrupole moment of CO_2. CH_4 is a nonpolar molecule which adsorbs on the surface by van der Waals forces [60].

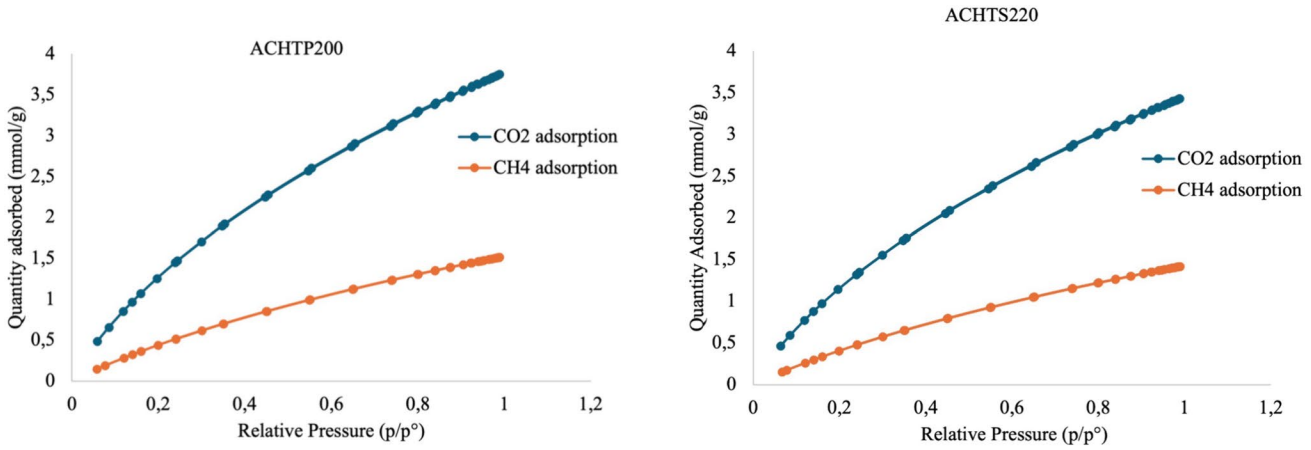

Fig. 9 CO_2 and CH_4 adsorption isotherms at 25 °C and up to 1 atm

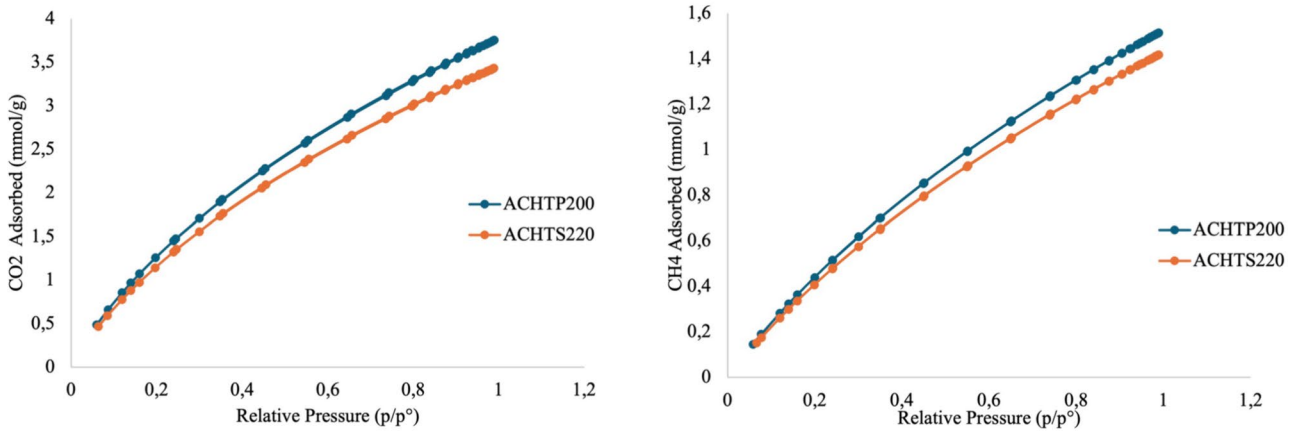

Fig. 10 **a** CO_2 **b** CH_4 adsorption isotherms for ACHTP200 and ACHTS220 at 25 °C and up to 1 atm

On the contrary, CO_2 is a polar molecule with a quadrupole moment of $13{,}4 \times 10^{-40}$ C.m^2, which enhances the electrostatic interaction between CO_2 and activated carbon's surface functional groups at low pressures [14, 69, 70]. Besides, CO_2 has a kinetic diameter (0,33 nm) less than that of CH_4 (0,38 nm), which favors the diffusion capability of CO_2 through the pores [71].

As seen in Fig. 10, ACHTP200 adsorbed more CO_2 and CH_4 compared to ACHTS220. The main reasons for this can be: (I) The specific surface area of ACHTP200 is higher than that of ACHTS220 (see Table 3). (II) Although they have the same surface functional groups, more functional groups are present on the surface of ACHTP200 (see Supplementary Fig. A1). (III) ACHTP200 has more micropores with diameters smaller than 1 nm (see Supplementary Fig. A2).

The CO_2 adsorption capacity of the activated hydrochars obtained in this study was compared with that of similarly synthesized activated carbons (see Table 3). The results indicate that the activated hydrochars from sawdust have a high CO_2 adsorption capacity, making them suitable for CO_2 adsorption at atmospheric temperature and pressure.

Both ACHTP200 and ACHTS220 showed better CH_4 adsorption capacity at low pressure as compared to other experimental studies such as Saha et al. [76], Reljic et al. [77], and Ariyanto et al. [78]. For high methane adsorption, it is necessary to have both a predominantly microporous structure and a small amount of mesopores. In addition to their high surface area and microporous structure, activated hydrochars with a small amount of mesopores showed high CH_4 adsorption capacity. Since the use of active hydrochars in CH_4 adsorption at atmospheric temperature and pressure has not been studied so far, Table 4 only shows the CH_4 adsorption capacity of activated carbons obtained directly from biomass. As seen in Table 4, the active hydrochars obtained in this study have higher CH_4 adsorption capacity than other activated carbons.

Table 3 Comparative study of CO_2 adsorption for different biomass samples

Precursor	HTC conditions	Carbonization conditions	Activation conditions	CO_2 adsorption	Ref
Rambutan peel	170 °C, 90 min	–	*850 °C KOH:HC = 2:1 120 min	278 mmol/g, 30 ^{O}C, 1 atm	Zubbri et al. [72]
Garlic peel	200 °C, 24 h	400 °C, 2 h	600 °C KOH:HC = 2:1 60 min	42 mmol/g; 25 ^{O}C, 1 atm	Huang et al. [73]
Chitosan	180 °C, 24 h	300 °C, 4 h	600 °C KOH:HC = 2:1 60 min	441 mmol/g; 25 ^{O}C, 1 atm	Wang et al. [74]
Orange peel	220 °C, 3 h	–	*700 °C KOH:HC = 3:1 120 min	3045 mmol/g; 25 ^{O}C, 1 atm	Deepak et al. [75]
Poplar sawdust	200 °C, 90 min	–	*800 °C KOH:HC = 2:1 60 min	3753 mmol/g; 25 ^{O}C, 1 atm	This study
Spruce sawdust	220 °C, 90 min	–	*800 °C KOH:HC = 2:1 60 min	343 mmol/g; 25 ^{O}C, 1 atm	This study

*Simultaneous activation and carbonization

Table 4 Comparative study of CH_4 adsorption for different biomass samples

Precursor	HTC	Activation conditions	Carbonization conditions	CH_4 adsorption	References
Coconut shell charcoal	–	1 M H_3PO_4, (2 ml acid/g precursor), 80 °C, 2 h	500 °C, under N_2, 2 h	0,256 mmol/g; 10 °C; atmospheric pressure	Song et al. [79]
Coconut shell charcoal	–	0,5 M KOH, (2 ml acid/g precursor), 80 °C, 2 h	600 °C, under N_2, 2 h	0,25 mmol/g; 10 °C; atmospheric pressure	
Palm sheath	–	KOH:biomass = 1:1	550 °C, under N_2, 1 h	1,02 mmol/g; 25 °C, 1 bar	Zhang et al. [80]
Palm sheath	-	KOH:biomass = 2:1	650 °C, under N_2, 1 h	1,47 mmol/g; 25 °C, 1 bar	
Palm sheath	-	KOH:biomass = 3:1	750 °C , under N_2, 1 h	0,98 mmol/g; 25 °C, 1 bar	
Poplar sawdust	200 °C, 90 min	KOH:hydrochar = 2:1	*800 °C , under N_2, 60 min	1,52 mmol/g; 25 °C, 1 atm	This study
Spruce sawdust	220 °C, 90 min	KOH:hydrochar = 2:1	*800 °C, under N_2, 60 min	1,42 mmol/g; 25 °C, 1 atm	This study

*Simultaneous activation and carbonization

4 Conclusions

In this study, wood sawdust, a locally abundant waste product, was successfully converted into activated hydrochar for CO_2 and CH_4 adsorption. The key findings are as follows:

1 . Impact of Hydrothermal Carbonization: HTC enriched the carbon content in both poplar and spruce sawdust, with notable shifts in the H/C and O/C ratios, particularly at 200 °C for poplar and 220 °C for spruce. This indicates that HTC effectively promoted carbon enrichment and partial hydrogen removal.

2 . Activation-Carbonization Process: The one-step activation-carbonization process with KOH significantly

enhanced the carbon structure, reducing the atomic H/C ratio (< 0,15) and modifying the surface properties with a notable presence of oxygenated functional groups.

3 . Pore Structure and Surface Properties: Regardless of HTC application, the average pore diameter of activated carbons obtained from wood sawdust was between 0,98 and 1,09 nm.

4 . Adsorption Capacities: ACHTP200 and ACHTS220, with their higher surface area and pore volume, demonstrated high CO_2 and CH_4 adsorption capacities at 25 °C and 1 atm.

5 . Application Potential: Despite their high adsorption capacities, these activated carbons are not suitable for CO_2-CH_4 separation. However, they show promise for applications such as indoor air quality improvement and capturing emissions from industrial point sources.

This study highlights the potential of converting wood sawdust into high-value activated carbons for environmental applications, emphasizing the role of HTC and activation processes in determining the final properties and performance of the adsorbents.

Supplementary Information The online version contains supplementary material available at https://doi.org/10.1007/s10450-024-00542-y.

Acknowledgements This research did not receive any specific grant from funding agencies in the public, commercial, or not-for-profit sectors.

Author contribution S.Basakcilardan Kabakci, B. Karakurt Cevik and M.N Borand organized the experimental design; M.N Borand collected the feedstock; B. Karakurt Cevik, M.N Borand and K. Al made experiments and analysis; S.Basakcilardan Kabakci, B. Karakurt Cevik and M.N Borand made data organizing, all authors wrote the draft of the manuscript and S.Basakcilardan Kabakci reviewed and editted.

Data availability No datasets were generated or analysed during the current study.

Declarations

Conflict of interest The authors declare no competing interests.

Ethical approval Not applicable. The research did not involve human participants or animals.

Consent to participate Not applicable.

Consent to publish Not applicable.

References

1. Chen, S., et al.: High adsorption selectivity of activated carbon and carbon molecular sieve boosting CO_2/N_2 and CH_4/N_2 separation. Chin. J. Chem. Eng. **67**, 282–297 (2024). https://doi.org/10.1016/j.cjche.2023.10.015
2. Li, K., Lin, B.: Impacts of urbanization and industrialization on energy consumption/CO_2 emissions: does the level of development matter? Renew. Sustain. Energy Rev. **52**, 1107–1122 (2015). https://doi.org/10.1016/j.rser.2015.07.185
3. Li, Y., Chen, B., Gao, Y., Zhang, J., Wang, B.: Optimization performance of viscose rayon derived flexible porous carbon cloths in relation to their CO_2 capture, CO_2/CH_4 separation and methanol adsorption. Coll. Surf Physicochem. Eng. Aspects **677**, 132350 (2023). https://doi.org/10.1016/j.colsurfa.2023.132350
4. Summary for Policymakers. (2022). In: Intergovernmental Panel on Climate C (eds) Global Warming of 15°C: IPCC Special Report on Impacts of Global Warming of 15°C above Pre-industrial Levels in Context of Strengthening Response to Climate Change, Sustainable Development, and Efforts to Eradicate Poverty. Cambridge University Press, Cambridge, pp 1–24
5. Das, A., et al.: Advancements in adsorption based carbon dioxide capture technologies–a comprehensive review. Heliyon (2023). https://doi.org/10.1016/j.heliyon.2023.e22341
6. Karimi, M., Shirzad, M., Silva, J.A.C.: Rodrigues AE Carbon dioxide separation and capture by adsorption: a review. Environ. Chem. Lett. **21**(4), 2041–2084 (2023). https://doi.org/10.1007/s10311-023-01589-z
7. You, Y.Y., Liu, X.J.: Performance comparison among three types of adsorbents in CO_2 adsorption and recovery from wet flue gas. Sep. Purif. Technol. **257**, 117922 (2021). https://doi.org/10.1016/j.seppur.2020.117922
8. Hamyali, H., Nosratinia, F., Rashidi, A., Ardjmand, M.: Anthracite coal-derived activated carbon as an effectiveness adsorbent for superior gas adsorption and CO_2/N_2 and CO_2/CH_4 selectivity: Experimental and DFT study. J. Environ. Chem. Eng. **10**(1), 107007 (2022). https://doi.org/10.1016/j.jece.2021.107007
9. Zhu, S., Zhao, B., Zhang, H.: Su Y biomass-based adsorbents for post-combustion CO2 capture: preparation, performances, modeling, and assessment. J. Environ. Manage. **328**, 117020 (2023). https://doi.org/10.1016/j.jenvman.2022.117020
10. Wen, C., et al.: Biochar as the effective adsorbent to combustion gaseous pollutants: preparation, activation, functionalization and the adsorption mechanisms. Prog. Energy Combust. Sci. **99**, 101098 (2023). https://doi.org/10.1016/j.pecs.2023.101098
11. Gao, Y., Yue, Q., Gao, B.: Li A Insight into activated carbon from different kinds of chemical activating agents: a review. Sci. Total. Environ. **746**, 141094 (2020). https://doi.org/10.1016/j.scitotenv.2020.141094
12. Subramaniam, T., Ansari, M.N.M., Krishnan, S.G.: Khalid M Kenaf-based activated carbon: a sustainable solution for high-performance aqueous symmetric supercapacitors. Chemosphere **354**, 141593 (2024). https://doi.org/10.1016/j.chemosphere.2024.141593
13. Singh, G., Maria Ruban, A., Geng, X., Vinu, A.: Recognizing the potential of K-salts, apart from KOH, for generating porous carbons using chemical activation. Chem. Eng. J. **451**, 139045 (2023). https://doi.org/10.1016/j.cej.2022.139045
14. Abd, A.A., Othman, M.R., Kim, J.: A review on application of activated carbons for carbon dioxide capture: present performance, preparation, and surface modification for further improvement. Environ. Sci. Pollut. Res. **28**(32), 43329–43364 (2021). https://doi.org/10.1007/s11356-021-15121-9
15. Raeesh Muhammad, Yoon-Chae Nah, Hyunchul Oh (2023). Spider silk-derived nanoporous activated carbon fiber for CO2 capture and CH4 and H2 storage. J CO_2 Util 69: 102401 https://doi.org/10.1016/j.jcou.2023.102401
16. Benzigar, M.R., et al.: Recent advances in functionalized micro and mesoporous carbon materials: synthesis and applications. Chem. Soc. Rev. **47**(8), 2680–2721 (2018). https://doi.org/10.1039/C7CS00787F

17. Zhang, Z., Cano, Z.P., Luo, D., Dou, H., Yu, A.: Chen Z rational design of tailored porous carbon-based materials for CO_2 capture. J. Mater. Chem. A **7**(37), 20985–21003 (2019). https://doi.org/10.1039/C9TA07297G
18. Patel, H.A., Byun, J., Yavuz, C.T.: Carbon dioxide capture adsorbents: chemistry and methods. Chemsuschem **10**(7), 1303–1317 (2017). https://doi.org/10.1002/cssc.201601545
19. Singh, G., et al.: Emerging trends in porous materials for CO_2 capture and conversion. Chem. Soc. Rev. **49**(13), 4360–4404 (2020). https://doi.org/10.1039/D0CS00075B
20. Rombaldo, C.F.S., Lisboa, A.C.L., Mendez, M.O.A.: Coutinho AR Brazilian natural fiber (jute) as raw material for activated carbon production. Anais Da Academia Brasileira De Ciencias **86**(4), 2137–2144 (2014). https://doi.org/10.1590/0001-3765201420140143
21. Siipola, V., et al.: Effects of biomass type, carbonization process, and activation method on the properties of bio-based activated carbons. BioResources **13**(3), 5976–6002 (2018)
22. Tu, W., et al.: A novel activation-hydrochar via hydrothermal carbonization and KOH activation of sewage sludge and coconut shell for biomass wastes: preparation, characterization and adsorption properties. J. Coll. Interf. Sci. **593**, 390–407 (2021). https://doi.org/10.1016/j.jcis.2021.02.133
23. Liu, F.Y., Yu, R.D., Ji, X.D., Guo, M.H.: Hydrothermal carbonization of holocellulose into hydrochar: structural, chemical characteristics, and combustion behavior. Bioresour. Technol. **263**, 508–516 (2018). https://doi.org/10.1016/j.biortech.2018.05.019
24. Khan, T.A., Saud, A.S., Jamari, S.S., Ab Rahim, M.H., Park, J.W.: Kim HJ Hydrothermal carbonization of lignocellulosic biomass for carbon rich material preparation: a review. Biomass Bioenerg. **130**, 16 (2019). https://doi.org/10.1016/j.biombioe.2019.105384
25. Nizamuddin, S., et al.: An overview of effect of process parameters on hydrothermal carbonization of biomass. Renew. Sustain. Energy Rev. **73**, 1289–1299 (2017). https://doi.org/10.1016/j.rser.2016.12.122
26. Shen, Y.: A review on hydrothermal carbonization of biomass and plastic wastes to energy products. Biomass Bioenergy **134**, 105479 (2020). https://doi.org/10.1016/j.biombioe.2020.105479
27. Rasam, S., Keshavarz Moraveji, M., Soria-Verdugo, A., Salimi, A.: Synthesis, characterization and absorbability of Crocus sativus petals hydrothermal carbonized hydrochar and activated hydrochar. Chem. Eng. Process. Process Intensif. **159**, 108236 (2021). https://doi.org/10.1016/j.cep.2020.108236
28. Xu, J., Fan, Z., Yang, Q., Lu, G., Liu, P.: Wang D hydrothermal carbonization of waste wood: sustainable recycling of biomass by-products and novel performance enhancer for bitumen. Constr. Build. Mater. **404**, 133307 (2023). https://doi.org/10.1016/j.conbuildmat.2023.133307
29. Li, H., et al.: The effects of temperature and color value on hydrochars' properties in hydrothermal carbonization. Bioresour. Technol. **249**, 574–581 (2018). https://doi.org/10.1016/j.biortech.2017.10.046
30. Lu, X.W., Pellechia, P.J., Flora, J.R.V., Berge, N.D.: Influence of reaction time and temperature on product formation and characteristics associated with the hydrothermal carbonization of cellulose. Bioresour. Technol. **138**, 180–190 (2013). https://doi.org/10.1016/j.biortech.2013.03.163
31. Sluiter A Determination of structural carbohydrates and lignin in biomass [electronic resource] : laboratory analytical procedure (LAP) : issue date, 4/25/2008 / A. Sluiter ... [et al.]. National Renewable Energy Laboratory, Golden, Colo (2008).
32. Garcia, R., Pizarro, C., Lavin, A.G., Bueno, J.L.: Biomass proximate analysis using thermogravimetry. Bioresour. Technol. **139**, 1–4 (2013). https://doi.org/10.1016/j.biortech.2013.03.197
33. Buendia-Kandia, F., et al.: Hydrothermal conversion of wood, organosolv, and chlorite pulps. Biomass Convers Biorefin **10**(1), 1–13 (2020). https://doi.org/10.1007/s13399-019-00395-4
34. Park, S., Baker, J.O., Himmel, M.E., Parilla, P.A.: Johnson DK Cellulose crystallinity index: measurement techniques and their impact on interpreting cellulase performance. Biotechnol. Biofuels **3**(1), 10 (2010). https://doi.org/10.1186/1754-6834-3-10
35. Hoekman, S.K., Broch, A., Robbins, C., Zielinska, B., Felix, L.: Hydrothermal carbonization (HTC) of selected woody and herbaceous biomass feedstocks. Biomass Convers. Biorefin. **3**(2), 113–126 (2013). https://doi.org/10.1007/s13399-012-0066-y
36. Cheng, S.C., Huang, A.M., Wang, S.N., Zhang, Q.H.: Effect of different heat treatment temperatures on the chemical composition and structure of chinese fir wood. BioResources **11**(2), 4006–4016 (2016). https://doi.org/10.15376/biores.11.2.4006-4016
37. Yan, W., Perez, S., Sheng, K.C.: Upgrading fuel quality of moso bamboo via low temperature thermochemical treatments Dry torrefaction and hydrothermal carbonization. Fuel **196**, 473–480 (2017). https://doi.org/10.1016/j.fuel.2017.02.015
38. Zhuang, J., Li, M., Pu, Y., Ragauskas, A.J., Yoo, C.G.: Observation of potential contaminants in processed biomass using fourier transform infrared spectroscopy. Appl. Sci. **10**(12), 4345 (2020). https://doi.org/10.3390/app10124345
39. Reza, M.T., Wirth, B., Luder, U., Werner, M.: Behavior of selected hydrolyzed and dehydrated products during hydrothermal carbonization of biomass. Bioresour. Technol. **169**, 352–361 (2014). https://doi.org/10.1016/j.biortech.2014.07.010
40. Li, J., Zhao, P., Li, T., Lei, M., Yan, W.: Ge S Pyrolysis behavior of hydrochar from hydrothermal carbonization of pinewood sawdust. J. Anal. Appl. Pyrolysis **146**, 104771 (2020). https://doi.org/10.1016/j.jaap.2020.104771
41. Heidari, M., Dutta, A., Acharya, B., Mahmud, S.: A review of the current knowledge and challenges of hydrothermal carbonization for biomass conversion. J. Energy Inst. **92**(6), 1779–1799 (2019). https://doi.org/10.1016/j.joei.2018.12.003
42. Wang, T.F., Zhai, Y.B., Zhu, Y., Li, C.T.: Zeng GM A review of the hydrothermal carbonization of biomass waste for hydrochar formation: Process conditions, fundamentals, and physicochemical properties. Renew. Sustain. Energy Rev. **90**, 223–247 (2018). https://doi.org/10.1016/j.rser.2018.03.071
43. Coronella, C.J., Lynam, J.G., Reza, M.T.: Uddin MH Hydrothermal Carbonization of Lignocellulosic Biomass. In: Jin, F. (ed.) Application of Hydrothermal Reactions to Biomass Conversion, pp. 275–311. Springer, Berlin Heidelberg, Berlin, Heidelberg (2014)
44. He, Q., Cheng, C., Raheem, A., Ding, L., Shiung Lam, S., Yu, G.: Effect of hydrothermal carbonization on woody biomass: from structure to reactivity. Fuel **330**, 125586 (2022). https://doi.org/10.1016/j.fuel.2022.125586
45. Ando, H., Sakaki, T., Kokusho, T., Shibata, M., Uemura, Y., Hatate, Y.: Decomposition behavior of plant biomass in hot-compressed water. Ind. Eng. Chem. Res. **39**(10), 3688–3693 (2000). https://doi.org/10.1021/ie0000257
46. Maaoui, A., et al.: Assessment of pine wood biomass wastes valorization by pyrolysis with focus on fast pyrolysis biochar production. J. Energy Inst. **108**, 101242 (2023). https://doi.org/10.1016/j.joei.2023.101242
47. Ochieng, R., Cerón, A.L., Konist, A.: Sarker S A combined analysis of the drying and decomposition kinetics of wood pyrolysis using non-isothermal thermogravimetric methods. Energy Convers Manage: X **20**, 100424 (2023). https://doi.org/10.1016/j.ecmx.2023.100424
48. Li, J., et al.: Pyrolysis characteristics and non-isothermal kinetics of waste wood biomass. Energy **226**, 120358 (2021). https://doi.org/10.1016/j.energy.2021.120358

49. Slopiecka, K., Bartocci, P.: Fantozzi F Thermogravimetric analysis and kinetic study of poplar wood pyrolysis. Appl. Energy **97**, 491–497 (2012). https://doi.org/10.1016/j.apenergy.2011.12.056
50. Ding, Y., Ezekoye, O.A., Lu, S., Wang, C.: Zhou R Comparative pyrolysis behaviors and reaction mechanisms of hardwood and softwood. Energy Convers. Manage. **132**, 102–109 (2017). https://doi.org/10.1016/j.enconman.2016.11.016
51. Poletto, M., Zattera, A.J., Forte, M.M.C.: Santana RMC Thermal decomposition of wood: Influence of wood components and cellulose crystallite size. Bioresour. Technol. **109**, 148–153 (2012). https://doi.org/10.1016/j.biortech.2011.11.122
52. Yao, Z., Ma, X.: Hydrothermal carbonization of Chinese fan palm. Bioresour. Technol. **282**, 28–36 (2019). https://doi.org/10.1016/j.biortech.2019.02.130
53. Popescu, C.-M., Singurel, G., Popescu, M.-C., Vasile, C., Argyropoulos, D.S.: Willför S Vibrational spectroscopy and X-ray diffraction methods to establish the differences between hardwood and softwood. Carbohydr. Polym. **77**(4), 851–857 (2009). https://doi.org/10.1016/j.carbpol.2009.03.011
54. Bay, M.S., Karimi, K., Nasr Esfahany, M.: Kumar R Structural modification of pine and poplar wood by alkali pretreatment to improve ethanol production. Ind. Crops Prod. **152**, 112506 (2020). https://doi.org/10.1016/j.indcrop.2020.112506
55. Lichtenegger, H., Reiterer, A., Stanzl-Tschegg, S.E., Fratzl, P.: Variation of cellulose microfibril angles in softwoods and hardwoods—a possible strategy of mechanical optimization. J. Struct. Biol. **128**(3), 257–269 (1999). https://doi.org/10.1006/jsbi.1999.4194
56. Nitsos, C.K., Choli-Papadopoulou, T., Matis, K.A., Triantafyllidis, K.S.: Optimization of hydrothermal pretreatment of hardwood and softwood lignocellulosic residues for selective hemicellulose recovery and improved cellulose enzymatic hydrolysis. ACS Sustain. Chem. Eng. **4**(9), 4529–4544 (2016). https://doi.org/10.1021/acssuschemeng.6b00535
57. Chen, W., et al.: Insight into KOH activation mechanism during biomass pyrolysis: chemical reactions between O-containing groups and KOH. Appl. Energy **278**, 115730 (2020). https://doi.org/10.1016/j.apenergy.2020.115730
58. De Oliveira, L.H., Meneguin, J.G., Pereira, M.V., Do Nascimento, J.F., Arroyo, P.A.: Adsorption of hydrogen sulfide, carbon dioxide, methane, and their mixtures on activated carbon. Chem. Eng. Commun. **206**(11), 1533–1553 (2019). https://doi.org/10.1080/00986445.2019.1601627
59. Menya, E., Jjagwe, J., Kalibbala, H.M., Storz, H., Olupot, P.W.: Progress in deployment of biomass-based activated carbon in point-of-use filters for removal of emerging contaminants from water: a review. Chem. Eng. Res. Des. **192**, 412–440 (2023). https://doi.org/10.1016/j.cherd.2023.02.045
60. Petrovic, B., Gorbounov, M., Masoudi Soltani, S.: Impact of surface functional groups and their introduction methods on the mechanisms of CO_2 adsorption on porous carbonaceous adsorbents. Carbon Capture Sci Technol **3**, 100045 (2022). https://doi.org/10.1016/j.ccst.2022.100045
61. Islam, M.S., Ang, B.C., Gharehkhani, S.: Afifi ABM Adsorption capability of activated carbon synthesized from coconut shell. Carbon Lett **20**(1), 1–9 (2016). https://doi.org/10.5714/cl.2016.20.001
62. Njoku, V.O., Islam, M.A., Asif, M.: Hameed BH Adsorption of 2,4-dichlorophenoxyacetic acid by mesoporous activated carbon prepared from H3PO4-activated langsat empty fruit bunch. J. Environ. Manage. **154**, 138–144 (2015). https://doi.org/10.1016/j.jenvman.2015.02.002
63. Guo, Y., Wang, Q.: Fabrication and Characterization of Activated Carbon from Phyllostachys edulis Using Single -Step KOH Activation with Different Temperatures. Processes **10**(9), 1712 (2022). https://doi.org/10.3390/pr10091712
64. Shrestha, D.: Evaluation of physical and electrochemical performances of hardwood and softwood derived activated carbons for supercapacitor application. Mater. Sci. Energy Technol. **5**, 353–365 (2022). https://doi.org/10.1016/j.mset.2022.09.002
65. Opoku, B.K., Isaac, A., Micheal, A.A., Bentum, J.K., Muyoma, W.P.: Characterization of chemically activated carbons produced from coconut and palm kernel shells using SEM and FTIR analyses. Am. J. Appl. Chem. **9**(3), 90–96 (2021). https://doi.org/10.11648/j.ajac.20210903.15
66. Liang, Y., et al.: Preparation and hydrogen storage performance of poplar sawdust biochar with high specific surface area. Ind. Crops Prod. **200**, 116788 (2023). https://doi.org/10.1016/j.indcrop.2023.116788
67. Guy, M., et al.: Process parameters optimization, characterization, and application of koh-activated norway spruce bark graphitic biochars for efficient azo dye adsorption. Molecules **27**(2), 456 (2022). https://doi.org/10.3390/molecules27020456
68. Sing, K.S.W., et al.: Reporting physisorption data for gas solid systems with special reference to the determination of surface-area And Porosity (RECOMMENDATIONS 1984). Pure Appl. Chem. **57**(4), 603–619 (1985). https://doi.org/10.1351/pac198557040603
69. Dilokekunakul, W., Teerachawanwong, P., Klomkliang, N., Supasitmongkol, S.: Chaemchuen S Effects of nitrogen and oxygen functional groups and pore width of activated carbon on carbon dioxide capture: Temperature dependence. Chem. Eng. J. **389**, 124413 (2020). https://doi.org/10.1016/j.cej.2020.124413
70. Greco, G., Canevesi, R.L.S., Di Stasi, C., Celzard, A., Fierro, V.: Manyà JJ Biomass-derived carbons physically activated in one or two steps for CH_4/CO_2 separation. Renew. Energy **191**, 122–133 (2022). https://doi.org/10.1016/j.renene.2022.04.035
71. Inthawong, S., Wongkoblap, A., Intomya, W., Tangsathitkulchai, C.: The enhancement of co2 and ch4 capture on activated carbon with different degrees of burn-off and surface chemistry. Molecules **28**(14), 5433 (2023). https://doi.org/10.3390/molecules28145433
72. Zubbri, N.A., Mohamed, A.R., Lahijani, P.: Mohammadi M Low temperature CO_2 capture on biomass-derived KOH-activated hydrochar established through hydrothermal carbonization with water-soaking pre-treatment. J. Environ. Chem. Eng. **9**(2), 105074 (2021). https://doi.org/10.1016/j.jece.2021.105074
73. Huang, G.-g, Liu, Y.-f, Wu, X.-x, Cai, J.-j: Activated carbons prepared by the KOH activation of a hydrochar from garlic peel and their CO_2 adsorption performance. New Carbon Mater. **34**(3), 247–257 (2019). https://doi.org/10.1016/S1872-5805(19)60014-4
74. Wang, J., Chen, S., Jia-yu, Xu., Liu, L.-C., Zhou, J.-C., Cai, J.-J.: High-surface-area porous carbons produced by the mild KOH activation of a chitosan hydrochar and their CO2 capture. New Carbon Mater. **36**(6), 1081–1090 (2021). https://doi.org/10.1016/S1872-5805(21)60074-4
75. Deepak, K.R., Mohan, S., Dinesha, P., Balasubramanian, R.: CO_2 uptake by activated hydrochar derived from orange peel (*Citrus reticulata*): influence of carbonization temperature. J. Environ. Manage. **342**, 118350 (2023). https://doi.org/10.1016/j.jenvman.2023.118350
76. Saha, D., Fieback, T.M.: Tom B characteristics of methane adsorption in micro-mesoporous carbons at low and ultra-high pressure. Energ. Technol. **4**(11), 1392–1400 (2016). https://doi.org/10.1002/ente.201600172
77. Reljic, S., Cuadrado-Collados, C., Oliveira Jardim, E., Farrando-Perez, J., Martinez-Escandell, M.: Silvestre-Albero J Activated carbon materials with a rich surface chemistry prepared from L-cysteine amino acid. Fluid Phase Equilib. **558**, 113446 (2022). https://doi.org/10.1016/j.fluid.2022.113446
78. Ariyanto, T., Prasetyo, I., Mukti, N.F., Cahyono, R.B., Prasetya, A.: Nanoporous carbon based palm kernel shell and its characteristics of methane and carbon dioxide adsorption. Mater. Sci. Eng.

736(2), 022057 (2020). https://doi.org/10.1088/1757-899X/736/2/022057
79. Song, Y., Zhou, X., Wang, J.A.: Adsorption performance of activated carbon for methane with low concentration at atmospheric pressure. Energy Sources Part A **43**(11), 1337–1347 (2021). https://doi.org/10.1080/15567036.2019.1636903
80. Zhang, H.W., et al.: Efficient removal of Remazol brilliant blue R from water by a cellulose-based activated carbon. Int. J. Biol. Macromol. **207**, 254–262 (2022). https://doi.org/10.1016/j.ijbiomac.2022.02.174